Author for correspondence:
Ludovic Keiser
e-mail: ludovic.keiser@univ-cotedazur.fr

Embolism propagation in *Adiantum* leaves and in a biomimetic system with constrictions

Ludovic Keiser[1], Benjamin Dollet[2] and Philippe Marmottant[2]

[1]Université Côte d'Azur, CNRS, INPHYNI, Nice, France
[2]Université Grenoble Alpes, CNRS, LIPhy, Grenoble, France

LK, 0000-0002-1681-9606; BD, 0000-0002-1756-7543; PM, 0000-0001-6828-6656

Drought poses a significant threat to forest survival worldwide by potentially generating air bubbles that obstruct sap transport within plants' hydraulic systems. However, the detailed mechanism of air entry and propagation at the scale of the veins remains elusive. Building upon a biomimetic model of leaf which we developed, we propose a direct comparison of the air embolism propagation in *Adiantum* (maidenhair fern) leaves, presented in Brodribb *et al.* (Brodribb TJ, Bienaimé D, Marmottant P. 2016 Revealing catastrophic failure of leaf networks under stress. *Proc. Natl Acad. Sci. USA* **113**, 4865–4869 (doi:10.1073/pnas.1522569113)) and in our biomimetic leaves. In particular, we evidence that the jerky dynamics of the embolism propagation observed in *Adiantum* leaves can be recovered through the introduction of micrometric constrictions in the section of our biomimetic veins, mimicking the nanopores present in the bordered pit membranes in real leaves. We show that the intermittency in the propagation can be retrieved by a simple model coupling the variations of pressure induced by the constrictions and the variations of the volume of the compliant microchannels. Our study marks a step with the design of a biomimetic leaf that reproduces particular aspects of embolism propagation in real leaves, using a minimal set of controllable and readily tunable components. This biomimetic leaf constitutes a promising physical analogue and sets the stage for future enhancements to fully embody the unique physical features of embolizing real leaves.

1. Introduction

In plants, water is driven in the xylem by evapotranspiration from the roots to the leaves. This water ascent occurs mainly at negative pressure, and the hydraulic transport can be hindered by air embolism events. During droughts, the decrease in water supply owing to soil drying can fail to compensate for the evapotranspiration flux in the leaves, leading to a strong decrease of the water potential within the xylem and potentially to the obstruction of the conduits by air bubbles, thereafter called embolism. Embolism can severely decrease the sap conduction, and cause permanent damage in the plant productivity [1,2]. Recent evidence demonstrated a direct causality between embolism formation in leaves and the subsequent death of leaf tissues owing to cellular dehydration [3]. One of the main consequences of climate change is the increase in the intensity and frequency of drought events, threatening the survival of forests across the globe [4–6]. This underscores the critical need for an in-depth understanding of embolism propagation through the xylem, aiming to enhance predictability regarding the anatomical features of plants that fortify resistance against such climatic threats.

Modern technical developments have enabled to image embolism in various parts of the plants [7–9]. Optical methods have recently enabled researchers to detect live embolism propagation events. Those methods consist of observing the change in light transmission through leaf [10,11], root [12], stems [13] or reproductive organs [14] as their veins transition from being filled with liquid water to containing water vapour or air. While this method facilitates rapid tracking of embolism events with a temporal resolution of the order of 1 s or even finer, its applicability is primarily limited to tissues that are relatively transparent, given its reliance on the principles of light transmittance. For tissues lacking transparency, techniques such as X-ray tomography or nuclear magnetic resonance [15,16] have been effective in mapping the spatial distribution of water within trunks or branches over time, thereby revealing the gradual infiltration of air into the network. However, these methods are limited in their ability to provide the necessary time resolution required for real-time monitoring of fast embolism spreading.

A main feature described across a large amount of species and not really understood is the intermittency in the embolism growth, leading to a jerky propagation clearly visible when monitoring the embolism with optical methods [10,11]. From a physicist's perspective, the observed intermittency in embolism growth represents a striking departure from the smoother drying patterns in porous networks. The distinction primarily arises from the role of pit membranes in the xylem, which regularly impede the progression of embolism, thus contributing to the plant's drought resistance. These membranes are crucial in delaying air seeding, playing a key role in the plant's survival mechanisms. Understanding embolism propagation is therefore essential, as it would offer insights into the mechanisms of plant resistance, a subject of active scientific discussion. An air bubble within the xylem, driven by the environment of negative pressure, can rapidly expand until it reaches the next physical barrier, typically the end wall of the vessel or tracheid. These end walls are perforated by pores in the secondary cell walls, which house the pit membranes. These membranes feature nanopores that allow water passage while restricting air movement. The air is prevented from passing through the pit membrane until the pressure difference between adjacent conduits surpasses a specific threshold. This threshold can be quantitatively described by the Laplace equation, depending on the radius of the pore and the surface tension at the liquid–air interface.

Characterizing the intermittency of embolism propagation requires measurements spanning several orders of magnitude of time scales, with sub-second propagation through the pits followed by long periods of several minutes or hours during which the embolism does not progress. Furthermore, the process also involves several orders of magnitude of length scales, with embolism passing through nanoporous pit membranes and then rapidly invading millimetre-long conduits. This highly multi-scale aspect of the problem, coupled with the difficulty to image inside light-absorbing tissue, makes the real-time tracking of the embolism dynamics very challenging. This issue has motivated biomimetic approaches to simplify the study and thereby extract key essential physical ingredients.

Biomimetic approaches have proven to be useful to replicate key phenomena at stake in sap circulation [17], such as evapotranspiration [18], osmotic flows [19,20], negative pressure flows [21] or cavitation [22–25]. As an attempt to understand the physics ruling the sudden embolism propagation observed in real leaves, we designed in recent works a biomimetic leaf made of microchannels within a membrane made of polydimethylsiloxane (PDMS), a soft silicone-based polymer mimicking the compliant mesophyll of leaves. Following the design developed by Noblin *et al*. [18], we took advantage of water pervaporation through PDMS membranes to reproduce air embolism propagation in linear microchannels [26] and in more complex networks [27,28]. In a recent study, we demonstrated that an intermittency in the propagation of air embolism could be reproduced in biomimetic veins in PDMS, owing to the introduction of single constrictions in the channel width (of approx. 20 μm). Those constrictions reproduce the effect of biological pits in plant leaves [29] despite a simplification of the geometry compared with the complex three-dimensional fibrous geometries of real bordered pit membranes [30]. The strong deformations of the compliant channel induced by the variations of capillary pressure generated by the passage of embolism in the narrow constrictions was demonstrated to lead to jerky dynamics. Analogies with observations in real leaves were suggested, but a closer comparison between biological and biomimetic data was still missing. Here, we address the problem of the dynamics of propagation through multiple constrictions by studying linear channels composed of multiple constrictions in series. This linear geometry is reminiscent of the venation structure of the leaves of *Adiantum* (maidenhair fern), and closer comparisons are carried out with our biomimetic channels. This study represents a foundational step in understanding vascular network dynamics using simple linear fern-like biomimetic networks, with the intent to progressively extend our approach to more complex reticulate venation patterns characteristic of angiosperms.

In the first part, we detail some key features concerning the intermittency of the air seeding in real leaves of *Adiantum* characterized by bifurcation networks (§2). In this part, we provide an original analysis of data published by Brodribb *et al*. [10]. In the second part, we recall the intermittent dynamics occurring in PDMS biomimetic channels containing a single constriction. Building upon this design, we then experimentally explore the pervaporation dynamics in linear microchannels containing a number N_p of constrictions regularly distributed (§3). In a third part, we develop a model, based on pervaporation mass transfer and elasto-capillary coupling between the meniscus and the compliant microchannel, which rationalizes the dynamics and the role of constrictions (§4). In a final discussion (§5), we discuss the relevance of our biomimetic approach by comparing it with the measurements obtained from *Adiantum* leaves. Numerical simulations were carried out to account for dispersion in the constriction widths (or for phenotype variations in real leaves). Those simulations enable to demonstrate how slight anatomical variations lead to an enhanced scattering of the characteristic time scales owing to a leverage effect driven by the incomplete relaxation of the vein structure after the embolism passage through constrictions (or pits). It is noteworthy that our microfluidic model simplifies a vein as a singular conduit rather than reproducing the bundle of multiple aligned conduits typical in real plants. This simplification is discussed and contextualized in §5.3.

2. Air invasion in *Adiantum* leaves

The propagation of embolism in various species of leaves is intermittent and characterized by multiple successions of arrests and rapid propagations, as shown by Brodribb *et al.* [10,11]. We here focus on the case of *Adiantum* leaves, whose veins display a tree network topology, without loops (figure 1*a*). *Adiantum* leaves have been studied in [10], where the authors separated the leaf from its water supply by cutting the leaf at the base of the stipe and excising a pinna a few millimetres from the rachis. They then let it dry for a few hours. Images were captured at 15 s intervals using a low-magnification microscope. From these images, we performed our own analysis for the purpose of this article. We observed variations in light transmission, interpreted as the advancement of air through the leaf's venation system (see figure 1*b*). This approach, known as the optical vulnerability method, has been increasingly used over the last few years. Its efficacy in tracking embolism propagation within relatively transparent tissues has been well documented in a range of studies [3,10–12,14]. In our current approach, we have not accounted for potential variations in conduit lengths observed across various species [31]; our focus is primarily on measuring embolism dynamics through the characterization of times of arrest of the embolism.

We analysed the length $x = L_o - L$ of the air embolism invading each of the 22 leaf veins represented in figure 1*b*, L_o being the total length of a vein and L the remaining wet length. Air invasion proceeds by rapid steps of amplitude L_{jump}, and then halts for a time Δt (figure 2*a*). In figure 2*b*, we represent the waiting time Δt as a function of time for 12 veins. The graphs exhibit a general trend: the first arrest of the embolism is much longer than the following ones. Those data are averaged in the inset after classification based on their jump order n, from the first arrest ($n = 1$) to the last one ($n = 9$). A slightly growing trend for Δt can be distinguished from $n = 2$ to $n = 9$, but it is difficult to conclude owing to the dispersion of the data. Note that we considered as a first arrest ($n = 1$) the time between the branch cut and the first appearance of the embolism in the petiole. We here supposed that the drying time of the remaining water volume in the main branch (impossible to image) was small compared with the water volume in the leaves.

Note that in this experimental set-up, air enters the xylem from the cut petiole, leading to embolism propagation from the base of the pinna towards the leaf margins, as shown in figure 1*b*. This method, while accelerating the process for observation purposes, closely mirrors the natural progression of embolism in intact leaves from the petiole, thereby maintaining the relevance of our observations to real-leaf conditions. It is also interesting to note that embolism arrest points frequently align with network bifurcations (figure 1*b*). Although the prediction of individual embolism trajectories falls outside the direct scope of this article, future investigations could aim at determining whether these bifurcation points correspond to ends of conduits within the xylem network and how their spatial distribution might impact the spread of embolism [32,33].

The understanding of the physical mechanisms governing the jerky propagation of embolism and the distribution of waiting times is constrained by our current imaging capabilities, which cannot simultaneously resolve the dynamic processes at both the microscale and nanoscale in real time. Specifically, while 'static' imaging could successfully capture detailed structural features of the veins, live imaging of embolism events struggles to integrate both the high spatial resolution, needed to discern nanometric pit membranes and the broad temporal scales, from rapid events to slower, progressive changes. This inherent limitation arises from the need to balance between resolution and field of view, as well as between capturing fleeting dynamics and longer processes. Consequently, our purpose is to use simplified representations to focus on fundamental physical interactions within a more tractable experimental set-up. In that purpose, we now adopt a biomimetic approach using artificial silicone membranes mimicking the main features of *Adiantum* leaves, following our original experimental protocol [26,29].

3. Experiments in biomimetic linear channels

### 3.1. Silicone biomimetic leaf manufacturing and sample preparation

We first create a mould on a silicon wafer by using photolithography. A thin layer of thickness h of SU8 photoresist (provided by Gersteltec company) is insulated through a mask (provided by Selba company). The part of the resist which was shadowed from insulation by the mask is then washed out using a solvent (propylene glycol methyl ether acetate), leaving behind a patterned wafer, which will be our mould in the future steps. Once the wafer has been patterned, a layer of thickness H of liquid PDMS (Sylgard™ 184, from Dow company) is then deposited on the mould by spin coating. The liquid PDMS is then cured for 24 h at 65°C in an oven. The PDMS layer is then detached from the mould, and gently deposited on a glass slide, which was previously surface-treated using an atmospheric plasma cleaner. This suffices to bind the PDMS layer to the glass slide.

The channels are filled with deionized water by plunging the sample for 2 h in a water tank whose pressure is decreased below 70 cm Hg with a vacuum pump. Note that it is important to create a hole at the entry of the channel to enable direct liquid water entry, while the air stuck in the dead end is purged by air diffusion through the PDMS membrane. The experiment starts when the sample is released from the water-filled tank, superficially dried with absorbing paper, and placed under a microscope at ambient pressure to track the propagation of air embolism.

This protocol, developed by Noblin *et al.* [18] to study optimal evapotranspiration fluxes in real leaves and in leaf-like networks, was then revisited by Dollet *et al.* to study the propagation of air embolism in biomimetic leaf channels [26] and in simple biomimetic networks [27,28]. Recently, we obtained the first jerky propagation of air embolism in biomimetic microchannels by introducing a constriction in linear microchannels [29]. We first detail a bit further the physical mechanism behind this intermittency in the propagation of air embolism past a single constriction, before introducing the *Adiantum*-like network which we designed.
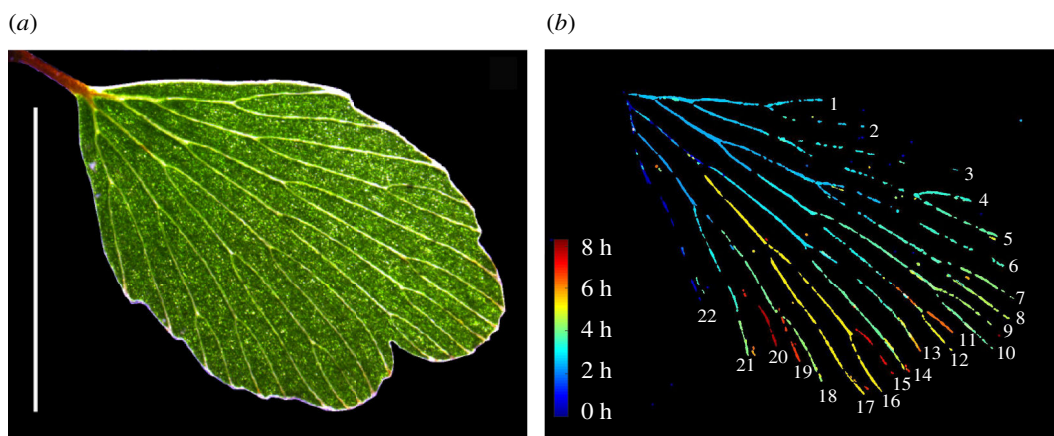
figure 1. Analysis carried out from the data shared by the authors of the reference [10], courtesy of Timothy Brodribb *et al.* (*a*) Leaf of the *Adiantum* fern (scale bar is 5 mm). (*b*) Detection of air embolism spreading in leaves within 22 veins. The colour represents the time at which they appear: dark blue at the start, dark red at the end (here after 8 h).
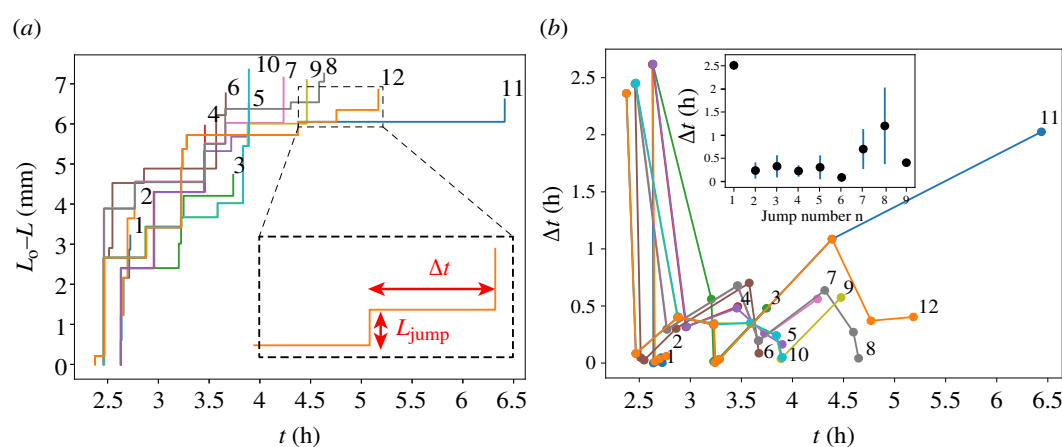

figure 2. Analysis carried out from the data shared by the authors of the reference [10], courtesy of Timothy Brodribb *et al.* (*a*) Length $L_o - L$ of the channel filled with air as a function of time for the first 12 veins. (*b*) Waiting time Δt before a jump in the first 12 veins of figure 1, as a function of time. Inset: Δt as a function of the jump number n.

Microchannels are thus formed within a PDMS medium (figure 3). The cross-section of the channels is rectangular, of width $w_o = 350$ μm and height $h = 73$ μm, and a total length L_o. The thickness of the PDMS membrane above the channel is denoted $\delta = H - h$. A number N_p of constrictions of width $w_p = 20$ μm and length $l_p = 180$ μm (horizontal ones) or $l_p = 300$ μm (vertical ones) are regularly distributed along the channel (figure 4), separating the total length of wide channels L_o into N_p cells of equal length $L_c = L_o/N_p$. In the experiments, the number of constrictions typically ranges from $N_p = 0$ to $N_p = 72$. Figure 3a represents the case $N_p = 1$, and figure 4 displays photographs of two channels with $N_p = 18$ for figure 4a and $N_p = 72$ for figure 4b.

3.2. Dynamics in a channel with a single pit-like constriction

In a recent study, we explored the dynamics of air invasion past a single constriction in a compliant microchannel [29] (figure 3), corresponding to the case $N_p = 1$. A dead-end microchannel, initially filled with water, is placed under a microscope. The small thickness of the PDMS membrane, of a few tens of micrometres, leads to a relatively fast pervaporation of the water content [34]. An air embolism can thus progressively grow to compensate the loss of the water content. While the air propagation was shown to be smooth in straight microchannels, following exponential relaxation laws, we demonstrated in [29] that this presence of a single constriction can lead to highly nonlinear dynamics (figure 3a). The air embolism interface is stopped at the exit of the constriction, for several minutes. After this waiting time Δt, the interface suddenly advances in the next channel by an amplitude L_{jump} in a few seconds. We demonstrated that the constriction forces the air–water interface to be curved, which leads to a strong decrease of the pressure in the liquid-filled channel owing to the capillary Laplace pressure difference at the interface. This induces the arrest in the propagation of air, as the loss of water by pervaporation is compensated by a compression of the compliant channel (figure 3c), owing to the decrease of the pressure. Once a threshold pressure is reached within the channel, depending on the width of the constriction w_p, the tension is released and the embolism can suddenly jump by an incremental length L_{jump}. This length was proven to follow a law given by water mass conservation during the jump,

$$L_{jump} = L_o \frac{\Delta S_c}{S_o}, \tag{3.1}$$
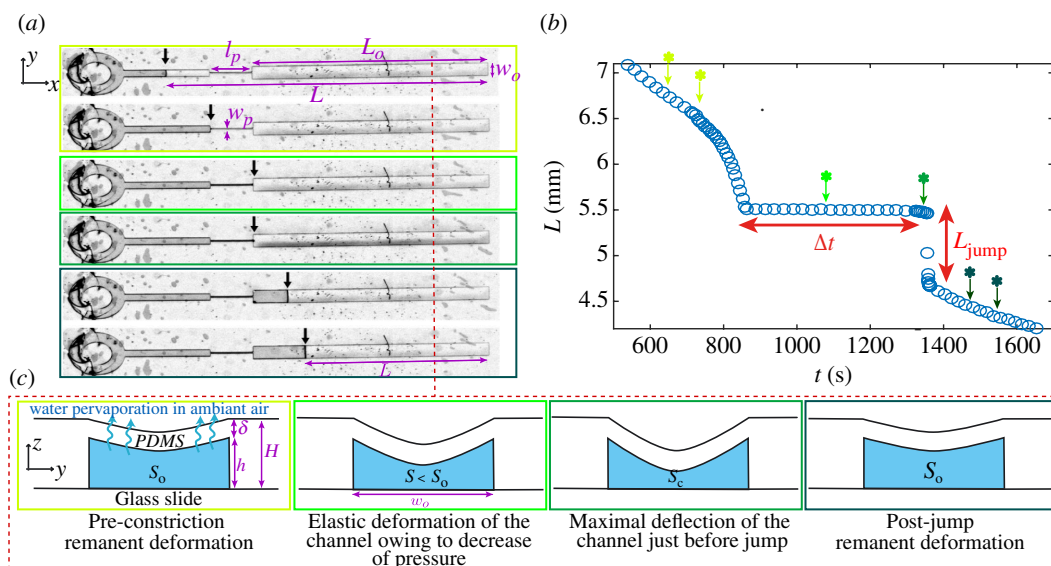
figure 3. Summary of the jerky dynamics observed in the presence of a single constriction during embolism invasion in linear channels characterized by $L_o = 5.5$ mm, $l_p = 1$ mm, $w_o = 390\,\mu$m, $w_p = 30\,\mu$m, $h = 65\,\mu$m and $H = 95\,\mu$m [29]. (a) Time lapse of an experiment of biomimetic channel drying by pervaporation. Nine hundred seconds separate the first image (top) and the last image (bottom). The length L of the liquid part (in light grey) gradually diminishes as the air embolism (in dark grey) progresses. (b) Time evolution of L during the passage of the interface through the constriction. It shows a marked arrest, during a time Δt, followed by a rapid jump of the interface of amplitude L_{jump}. The coloured stars correspond to the different moments of the time lapse in (a). (c) Sketch of the cross-section of the liquid-filled part of the channel (corresponding to the plane represented by the red-dashed line in panel (a)) at the different moments of the embolism propagation through the constriction. These sketches were confirmed by confocal imaging in [29].
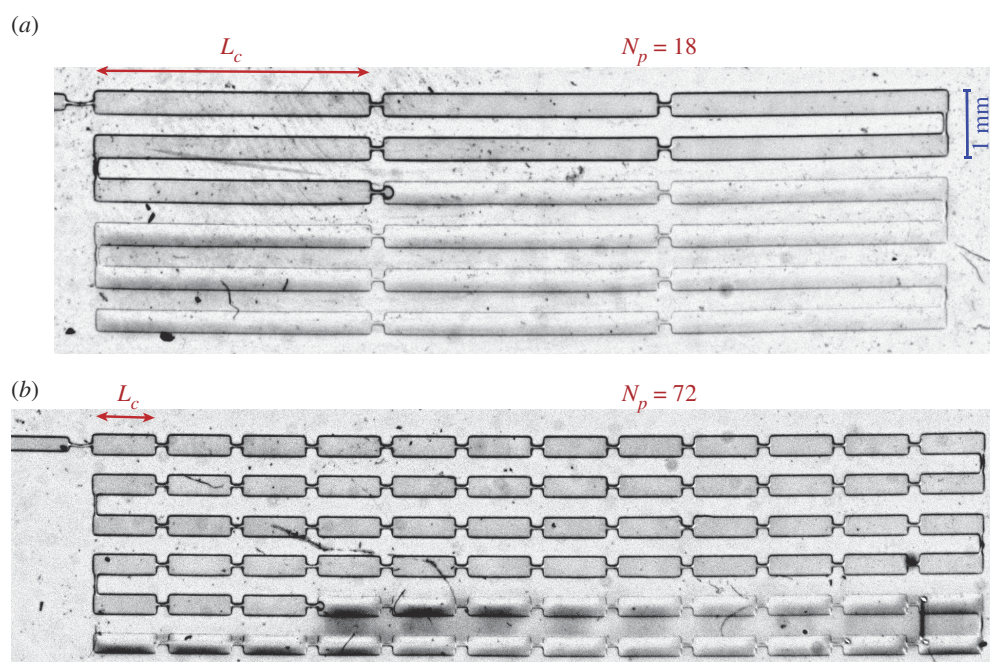
figure 4. Two linear channels of length $L_o = N_p L_c = 72$ mm and width $w_o = 350\,\mu$m, separated by a number $N_p = 18$ (a) and $N_p = 72$ (b) of constrictions of width $w_p = 20\,\mu$m and length $l_p = 180\,\mu$m (horizontal ones) or $l_p = 300\,\mu$m (vertical ones). The length of the cells is $L_c = L_o/N_p$. In these two pictures, the air embolism (channels in darker grey) penetrates, respectively, in the 8th and 52nd cell, which are still filled with water (lighter grey cells), as well as the rest of the channel until the dead end. The scale bar at the top right represents 1 mm.

where $\Delta S_c = S_o - S_c$ is the difference of area between the channel section before the embolism arrest in the constriction S_o and the minimal channel section just before the jump S_c. The intermittency thus originates from an elastocapillary coupling between the air embolism interface curvature generating pressure variations owing to its passage through the constriction, and the compliant structure of the channel, adapting its shape to the lower pressure imposed by the interface.

In the construction of our biomimetic model, it is pertinent to consider the wetting properties of the materials used. The contact angle of water on PDMS is approximately 110°, indicating a relatively hydrophobic surface. In contrast, water exhibits a contact angle close to 0° with glass, a highly hydrophilic surface. Given that the air–water interface in our model interacts with three PDMS walls (one long and two short ones) and one (long) glass wall, the overall wetting behaviour is quite favourable, resulting in an effective contact angle less than 90°. This set-up renders the channel partially wetting, albeit not as hydrophilic

as xylem walls in plants. Also, our previous work [29] has shown that a similar jerky propagation of embolism is observed even with fully wetting liquids like ethanol, indicating that the phenomenon is not heavily dependent on the specific wetting properties of the system.

3.3. Dynamics in the channel with multiple constrictions

The aforementioned jerky propagation was extensively studied in a channel with one single constriction mimicking pit membranes in real leaves. However, real leaves are composed of multiple channels separated by a high number of pits. We here explore a more complex configuration of a linear microchannel composed of successive constrictions, as a simple approximation of the venation of *Adiantum* leaves. In our experiments, we used samples with vessels of height $h = 73 \pm 2\mu$m, width $w_o = 350 \pm 10\mu$m and PDMS thickness $H = 86 \pm 2\mu$m. The number of constrictions N_p varies across our samples between 0 and 72. Figure 4 shows the top view for two experiments of air embolism propagation in linear veins with a number of constrictions $N_p = 18$ (top) and $N_p = 72$ (bottom) at the moment of the passage of an embolism past a constriction. The liquid-filled part appears in light grey and the air embolism appears in dark grey (light being less transmitted through the sample because the index of refraction of air is more different from PDMS than water is). The length of the embolism $x = L_o + N_p l_p - L$ (where $L_o + N_p l_p$ is the initial total length of liquid) is tracked and represented as a function of time in figure 5 for $N_p = 0$ (dark blue line, channel without constriction), $N_p = 18$ (light blue line) and $N_p = 72$ (yellow line). Three different dynamics can be observed:

— For $N_p = 0$, the progression is smooth and can be described by truncated exponential functions, as shown by Dollet *et al.* [26].
— For $N_p = 18$, the propagation of the embolism is stopped at each constriction during a time Δt, and then followed by a rapid jump of amplitude L_{jump} inside the next vessel (light blue line in figure 5). At the end of the jump, the embolism has not reached the next constriction; it then propagates smoothly, until reaching the next constriction and being arrested there again (figure 5b).
— For $N_p = 72$, the propagation of the embolism is much more jerky, and characterized by series of arrests and jumps at each constriction (figure 5). This peculiar propagation by steps is reminiscent of the observations in *Adiantum* leaves (figure 2a). Only for the very last moments is a smooth propagation recovered, when jumps are not long enough to reach the next constriction.

Considering the jump amplitude L_{jump}, figure 6 represents L_{jump} rescaled by the length of the individual vein elements $L_c = L_o/N_p$, as a function of the number n of the constriction where the jump occurs rescaled by the total number of constrictions. It enables to separate two classes of dynamics. For high numbers of constrictions ($N_p = 72$, empty triangles), the jump amplitude equals L_c for most of the constrictions and suddenly decreases for the last values of n/N_p. Conversely, for the channels with the lowest numbers of constrictions, L_{jump}/L_c decreases with n/N_p from the first constrictions onwards.

Considering the waiting time Δt, the results also show two classes of dynamics, see figure 7. For experiments with $N_p \leq 18$ (figure 7a), Δt appears constant during the experiment, regardless of the constriction order n. Note that the data are very scattered, a feature which we shall discuss in §5. For $N_p = 72$ (plotted separately for clarity on figure 7b), the first arrest at $\Delta t_o = 150$ s is of the order of those measured for $N_p \leq 18$. However, from the second constriction, the times of arrest Δt are much lower. And Δt appears to grow with n until reaching values of approximately 150 s again as $n \rightarrow N_p$. This change of monotonicity appears as a peculiar feature of channels composed of a high number of constrictions and for which the embolism propagates by steps, from one constriction directly to the other. In §4, we rationalize this effect. The solid lines in figures 6 and 7 correspond to predictions of the model, knowing the deformability of the channel $\Delta S_c/S_o$, measured using a confocal microscope.

Considering the time taken for the jump (figure 5b), it is noteworthy that it is considerably longer than what can be observed in real leaves (figure 2a). This difference is presumably owing to the viscoelastic nature of PDMS, which exhibits higher viscous characteristics than leaf tissue.

3.4. Insights from confocal imaging

We used a confocal microscope to determine the elastic deformation of the channel as a function of time. We diluted Sulforhodamine B, a fluorescent dye, in water to image the cross-section of the water-filled part of the channel, in a cell midway between two constrictions.

We measured the section area S of the channel as a function of time by using a confocal microscope, in the case $N_p = 3$ (figure 8a). We evidenced two distinct phases. A decrease of the section area S during a time interval Δt down to the critical section S_c, followed by a rapid restoration of the nominal S_o, corresponding to the jumps of the embolism. During the remaining time, the cross-section remains constant and equal to S_o, as the embolism interface is not pinned and propagates inside a vessel.

These measurements enable us to express the value of the deformability of the channel $\Delta S_c/S_o = (S_o - S_c)/S_o$, here estimated as $\Delta S_c/S_o = (8 \pm 1.5)\%$. Note that various measurement uncertainties are reducing the accuracy of the measurement, such as the time needed to span in the z-direction (approx. 30 s) during which the section is evolving owing to the ongoing pervaporation process.
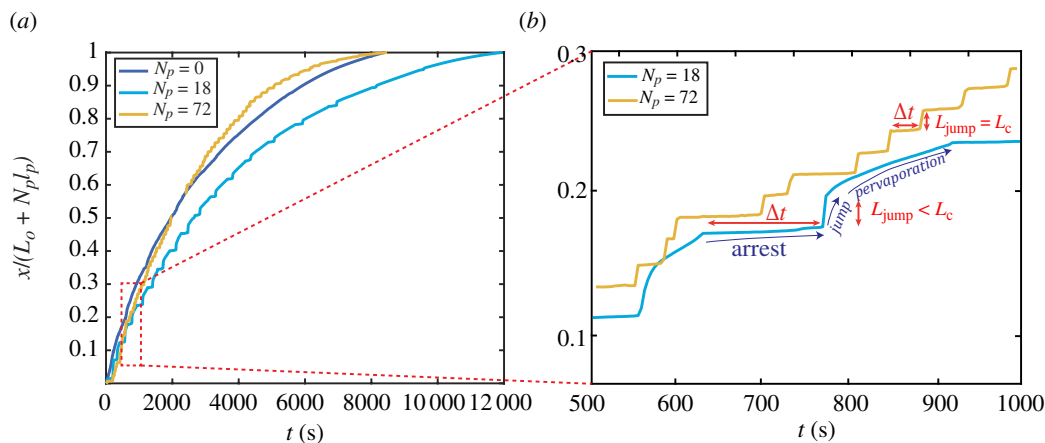
figure 5. Measurements of the time evolution of the length of the air embolism $x = L_o + N_p l_p - L$, rescaled by the total length $L_o + N_p l_p$. (a) Full embolism trajectory, from the first constriction ($x/(L_o + N_p l_p) = 0$) to the end of the channel ($x/(L_o + N_p l_p) = 1$), for three different values of $N_p = 72$ (yellow), 18 (light blue) and 0 (dark blue). (b) Zoom on the trajectory of the $N_p = 72$ and $N_p = 18$ cases. For $N_p = 72$ (yellow), the propagation only occurs by successive events of jumps and arrests. Conversely, for $N_p = 18$ (blue), the air embolism jumps inside a cell after a stop in a constriction, and then advances through smooth pervaporation process before being stopped at the next constriction. The double arrows define the variables Δt and L_{jump}, systematically measured in our study.
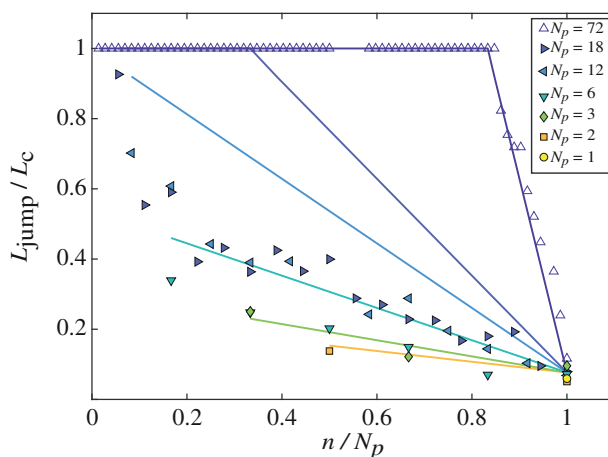
figure 6. L_{jump} normalized by the cell length L_c as a function of n/N_p. Two different classes of embolism dynamics emerge: (i) a jerky embolism propagation, where the interface jumps from one constriction to the other (empty triangles for $N_p = 72$) for most of the constrictions, except the very last ones. In this case, the elastic tension is only partially released after each jump; and (ii) a smoother propagation, for which the embolism never jumps directly from one constriction to the other (full markers, for $N_p \leq 18$). In this latter case, the elastic tension is completely released after each jump.
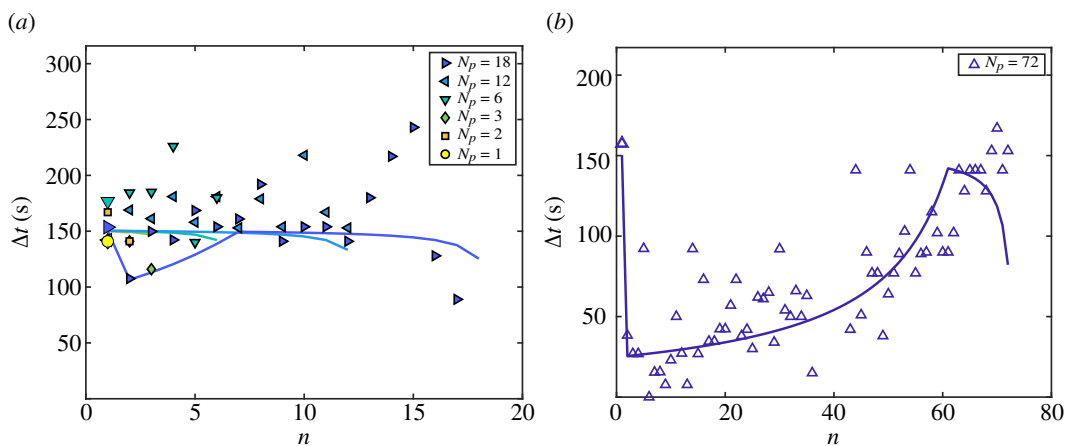
figure 7. Waiting time Δt as a function of the constriction order n. (a) With channels containing from 1 to 18 constrictions, the waiting time is nearly constant, although relatively scattered. This trend is confirmed by the predictions of the model of §4, represented in solid lines. (b) When the number of constrictions N_p is substantially increased (up to $N_p = 72$), the waiting time is maximal at the first constriction ($\Delta t \simeq 160$ s), drops down to $\Delta t \simeq 30$ s from the second constriction and then gradually increases up to $\Delta t \simeq 160$ s at the end of the experiment. For both panels, the solid lines represent the predictions of the model developed in §4, for a channel deformability $\Delta S_c/S_0 = 8\%$ and an initial waiting time at the first constriction $\Delta t_0 = 150.4$ s, taken as the average of the seven experimental data for N_p ranging from 1 to 72.
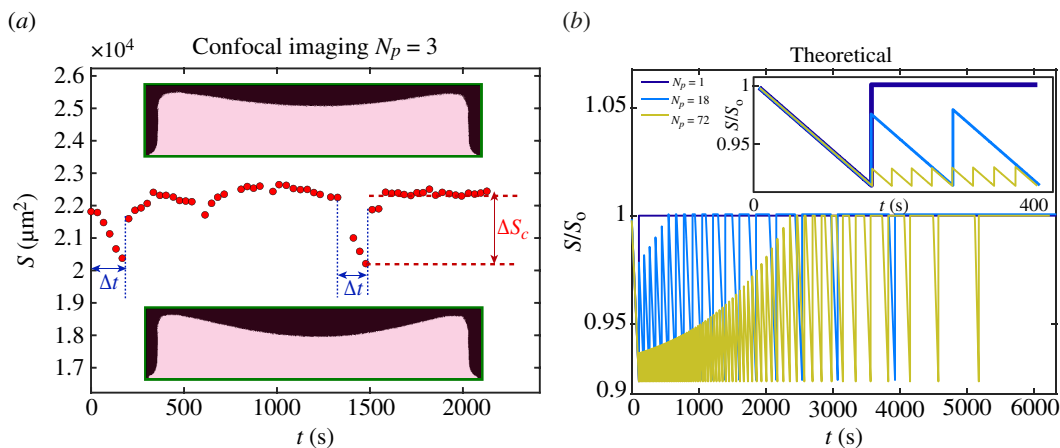
figure 8. (*a*) Surface area S of the channel cross-section as a function of time, measured by confocal imaging for the case $N_p = 3$. The two images in inset represent the measured cross-section of the channel just before a jump (bottom inset) and just after a jump (top inset). The difference of section area $\Delta S_c = S_o - S_c$ is directly linked to the amplitude of the jump L_{jump}. (*b*) S/S_o as a function of time derived using the model in §4 for three different numbers of constrictions: $N_p = 1$ (dark blue), $N_p = 18$ (light blue) and $N_p = 72$ (yellow). The dynamics was derived using the values of q_l and Q_g expressed in §4.

Predictions of the model developed in the next section are proposed in figure 8*b* as a comparison, and further discussed in §4.

4. Theoretical model and design rule

In linear microchannels, in the absence of constrictions, the embolism progression velocity is evolving progressively, and is solely influenced by the pervaporation dynamics [26]. Here, in the presence of constrictions, we propose to focus on the jump amplitudes and times of arrest only.

4.1. Model with N_p constrictions

We aim at predicting the waiting time Δt of the meniscus at each nth constriction. We call n the order of the constriction, where $n = 1$ corresponds to the first constriction to be encountered by the embolism front. N_p is the total number of constrictions in the channel, L_o the total length of the channel of width $w_o = 350\mu m$ and $L_c = L_o/N_p$ the length of each cell separated by constrictions.

The waiting time can be directly expressed, from mass conservation, as the ratio of the volume ΔV to evaporate before the jump to the volumetric flux of pervaporation. The waiting time at the nth constriction can be written

$$\Delta t_n = \frac{\Delta V_n}{q_l L_n + Q_g},\tag{4.1}$$

where $q_l = 1.70 \times 10^{-11}\ m^2\ s^{-1}$ and $Q_g = 1.45 \cdot 10^{-14}\ m^3\ s^{-1}$, respectively, represent the bulk pervaporation volumetric flux per unit length and the meniscus evaporation volumic flux. Those two values are independent on the position of the interface in the channel, and only depend on the geometry of the channel and on thermodynamic constants of the problem, as detailed in [26], where the formulae used for determining the numerical values of q_l and Q_g were established. The volume to pervaporate equals $\Delta V_n = L_n(S_n - S_c)$, with $L_n = L_o - (n-1)L_c$ the length of the water-filled channel, S_n the cross-section area (assumed uniform) of the water-filled channel at the beginning of the arrest in the nth constriction, and S_c the minimal area of the cross-section for which the jump is triggered. We neglect the volume of the constrictions in the analysis.

Hence, we obtain

$$\Delta t_n = \frac{S_n - S_c}{q_l + Q_g/L_n}.\tag{4.2}$$

The value S_n depends on whether the channel is fully relaxed when the meniscus reaches the nth constriction. The channel is assumed to be fully relaxed at the first constriction, and it is fully relaxed when the embolism reaches the other constrictions if they are not reached during a jump.

In the full relaxation case, $S_n = S_o$, and writing $\Delta S_c = S_o - S_c$, we have

$$\Delta t_n = \frac{\Delta S_c}{q_l + Q_g/L_n}.\tag{4.3}$$

In particular at the first constriction,

$$\Delta t_1 = \frac{\Delta S_c}{q_l + Q_g/L_o} = \Delta t_o.$$

For the other constrictions $n \geq 2$, one needs to check whether the previous jump directly reached the constriction. This is performed by comparing L_c with the amplitude $\mathcal{A}_{n-1}$ that the previous jump starting from constriction $n-1$ would have in the absence of constrictions,

$$\mathcal{A}_{n-1} = L_{n-1} \frac{\Delta S_c}{S_o}, \tag{4.4}$$

with

$$L_n = (N_p - n + 1) L_c. \tag{4.5}$$

Equation (4.4) translates the fact that the change of channel volume during complete relaxation draws a water volume that leads to an advance of meniscus through the air-filled part of the channel and having a section S_o. If $\mathcal{A}_{n-1} < L_c$, equation (4.3) holds, else the channel is not fully relaxed at the beginning of the arrest in the nth constriction.

In the case of an incomplete relaxation, the jump leads directly from the $(n-1)$th constriction, where $S = S_c$, to the nth constriction where $S = S_n$. The water volume conservation during the jump yields $S_n L_n = S_c L_{n-1}$, which, when injected in (4.2), yields

$$\Delta t = \frac{S_c}{q_l (N_p - n + 1) + Q_g / L_c}. \tag{4.6}$$

Using (4.4) and (4.5), the condition $\mathcal{A}_{n-1} < L_c$ is equivalent to $(N_p - n + 2)\Delta S_c / S_o < 1$, hence to $n > n_j$ with

$$n_j = 2 + N_p - \frac{S_o}{\Delta S_c}. \tag{4.7}$$

In summary, we have two expressions for the waiting time, depending on whether the channel has fully relaxed or not. Full relaxation is achieved at the first constriction, and

— if $n > n_j$ with n_j given by (4.7), the waiting time is then given by (4.3);
— if $2 \leq n \leq n_j$, the channel is only partially relaxed when the arrest begins at the nth constriction, and the waiting time is given by (4.6).

Crucially, the two expressions of the waiting time display opposite dependences on n: while in the full relaxation case, (4.3) is a decreasing function of n (all the more that $N_p - n$ tends to 0 as the effect of the meniscus evaporation flux becomes gradually more important compared with the bulk pervaporation term), in the partial relaxation case, (4.6) is an increasing function of n.

4.2. Comparison with the experiments

These predictions are in reasonable agreement with the experimental data, as shown in figure 6 and in figure 7a,b, where solid lines represent the model predictions with a deformability of the channel taken as $\Delta S_c / S_o = 8\%$, in agreement with observations made with the confocal microscope.

Concerning the area of the section of the water-filled parts of the channel during the propagation of the embolism, figure 8b provides a prediction of the model for the cases $N_p = 1$, $N_p = 18$ and $N_p = 72$. For $N_p = 1$ (dark blue line), a complete relaxation of the elastic energy occurs after the first and unique jump, and the area of the cross-section equals S_o just after the jumps. Conversely, for both $N_p = 18$ and $N_p = 72$, the first jumps lead to an incomplete relaxation of the elastic energy, owing to the arrest of the embolism interface at the next constriction, which leads to a subsequent elastic loading. Note that after a given number of constrictions corresponding to the parameter n_j obtained in equation (4.7), a complete elastic relaxation of the channel after each jump is recovered. This threshold value n_j is larger for $N_p = 72$ (yellow line) than for $N_p = 18$ (light blue line).

While the model accounts reasonably well for the value of n_j for $N_p = 72$ in the representation of L_{jump} versus n (figure 6), it overestimates the value of n_j for the case $N_p = 18$. Several reasons may explain this discrepancy, such as uncontrolled variations on the geometrical parameters h and H between the different veins. Furthermore, the deformability $\Delta S_c / S_o$ was measured by confocal microscopy for one channel and considered equal for all of them. While this assumption is correct if all the geometric parameters of the experiments are constant (with the exception of N_p and L_c which are varied), differences between channels may come from the membrane production protocol (photolithography, PDMS spin-coating, curing, membrane detachment and attachment). Section 5 is devoted to the quantification of the impact of this variability in the parameters on the measured times of arrest.

4.3. Design rule for a change of monotonicity in the Δt versus n curves

It is possible to distinguish the two classes of phenomenology depending on whether n_j is smaller or larger than 2. If $n_j \geq 2$, part of the embolism dynamics is characterized by a front directly jumping from one constriction to the next one. Consequently, the Δt versus n curve exhibits a change of monotonicity, with Δt brutally decreasing between $n = 1$ and $n = 2$, and then gradually increasing up to $\Delta t = \Delta t_0$. The second change of monotonicity can be observed as n tends to N_p if the meniscus evaporation term is large enough.

Conversely, if $n_j < 2$, no jump is large enough to reach directly the next constriction. The Δt vs n curve is then only smoothly decreasing, owing to the sole minor effect of the additional meniscus evaporation term.

This condition on the value of n_j can help us provide a design rule for the biomimetic channels. For a given number of constrictions, the change of monotonicity will be encountered if the deformability of the channels is larger than a critical value,

$$\frac{\Delta S_c}{S_o} \geq \frac{\Delta S_c^*}{S_o} = \frac{1}{N_p}. \tag{4.8}$$

Similarly, for a given deformability of the channel, the change of monotonicity in the Δt versus n curves will be encountered if the number of constrictions is larger than a critical value,

$$N_p \geq N_p^* = \frac{S_o}{\Delta S_c}. \tag{4.9}$$

This equivalence between increasing N_p or increasing the deformability of the channel to get a step-like propagation of the embolism is confirmed with the graphs presented in figure 9. For a given number of constrictions N_p, the change of monotonicity is more pronounced when $\Delta S_c/S_o$ is increased. Conversely, for a given deformability $\Delta S_c/S_o$, the change of monotonicity is more pronounced when the number of constrictions is increased from $N_p = 9$ (figure 9a) to $N_p = 72$ (figure 9b).

5. Comparison between biological and biomimetic data

In this section, we confront our results with the biological data obtained from the *Adiantum* leaves. We then discuss the strong scattering of the times of arrest Δt in the biomimetic channels, in spite of the precision of the design obtained by microphotolithography, and relate it to the dispersion observed in the data extracted from real leaves.

5.1. Comparing the times of arrest Δt

The model of §4 captures the dependence of the waiting time on the order n of the constriction shown by *Adiantum*, in particular the change of monotonicity between the first and the second constrictions. We recall that measurements with *Adiantum* show a very long first arrest, followed by much shorter waiting times (inset of figure 2). In artificial leaves, this trend is only observed when the compliance is large enough ($n_j > N_p/2$). In our work, large values of N_p had to be reached to observe a change of monotonicity in the Δt versus n curve, because the compliance of our channel was relatively weak.

Conversely, the biological data presented in figure 2b are such that the propagation of the embolism is always jumping from one constriction to the other, as if $n_j \simeq N_p$. According to our model, this fact implies that the compliance of the biological hydraulic system is large. In figure 10, the waiting times measured from *Adiantum* leaves are fitted by the model with $N_p = 9$. The best fit corresponds to a deformability of the channels $\Delta S_c/S_o = 58\%$. These observations could be linked to the strong contraction of the xylem structure when subjected to low pressure induced by a water stress [35–40]. However, in addition to the contraction of the veins induced by the decrease of the water pressure during drying, another source of capacitance in the hydraulic network could arise from the significant water content in the mesophyll surrounding the veins [41,42]. This condition could not be met with our biomimetic design, insofar as PDMS contains very little water. Interestingly, this echoes the role of 'bound water' in tissues surrounding water-conducting vessels, recently evidenced in the drying of wood [15] or of fabric [43]. Therefore, it is certainly too preliminary to interpret all the biological data with a model accounting solely for the deformation of the veins as the unique source of capacitance.

5.2. Impact of the variability of the constriction width w_p: numerical resolution

In order to understand the strong variability in waiting time observed in biomimetic data, and even stronger in biological data, we complexify our model by introducing a probability distribution for the threshold section S_c in our theoretical model.

We assume a normal distribution of the constriction size w_p, with a relative standard deviation $\overline{\sigma_{w_p}}$ varying between 0 and 20%. This distribution has an influence on the threshold ΔS_c linked to w_p through the following inverse relationship: $\Delta S_c = \phi/w_p$, where ϕ is a parameter accounting for the effect of surface tension γ, elastic modulus of PDMS E and geometric parameters of the channels and membranes δ, h and w_o. This inverse dependency was proven in our previous work [29] to originate from the fact that Laplace pressure is proportional to the inverse of the width of the constriction, and the deformation is proportional to the Laplace pressure.

For a distributed S_c, the system of equations presented in §4 can be solved numerically using a time finite-difference method. This numerical procedure enables to generate numerous runs of embolism growth and to characterize the effect of a statistical distribution of the blocking threshold S_c among the 72 constrictions of the simulated channel. We choose $N_p = 72$ to stick to the experimental case where the partial relaxation of the channel was evidenced (figures 6 and 7b). We present in figure 11a typical runs for different standard deviations σ_{w_p}. Remarkably, the dispersion of waiting times is large at the beginning, but decreases at increasing n. This is quantified in figure 11b, where we see a linear decrease of the standard deviation with n. The relative variability of waiting times $\overline{\sigma_{\Delta t}} = \sigma_{\Delta t}/\overline{\Delta t}$ is initially greatly enhanced compared with the relative variability of the
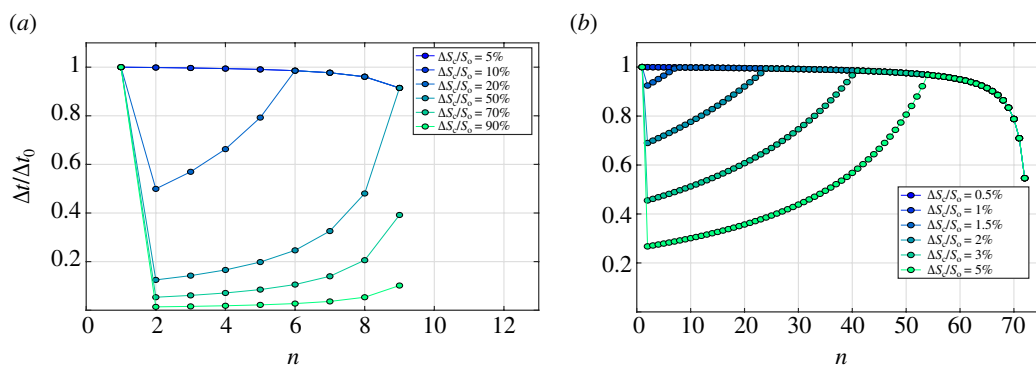
figure 9. Influence of the compliance of the hydraulic channel on the waiting time Δt. The different lines correspond to predictions of the model for different values of channel deformability $\Delta S_c/S_o = (S_o - S_c)/S_o$ before a jump, as indicated by the legends. The number of constrictions is (a) $N_p = 9$ (b) $N_p = 72$.
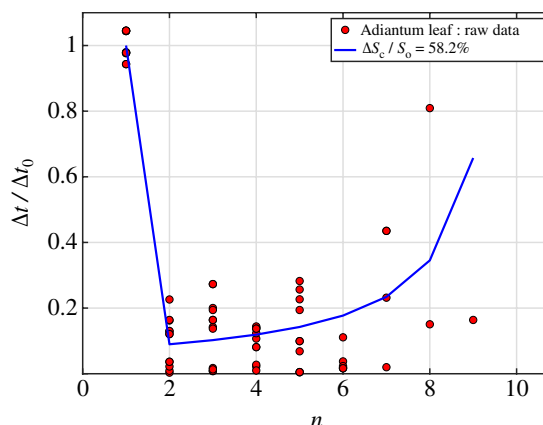
figure 10. Analysis carried out from the data shared by the authors of reference [10], courtesy of Timothy Brodribb *et al.* Comparison between the model (blue line) and biological data obtained with *Adiantum* leaves (red circles). For biological data, the waiting time Δt was rescaled by the mean value of the waiting time at the first pit, $\Delta t_0 = 2.5$ h. The best fit of the experimental point by the model is obtained for a deformability $\Delta S_c/S_o = 58\%$ and a number of pits $N_p = 9$. Note that the scattering of the measured values is even higher than what is observed in biomimetic data (compare with figure 7b).

constriction sizes $\overline{\sigma_{w_p}} = \sigma_{w_p}/\overline{w_p}$. For low values of N_p and $\Delta S_c/S_o$, $n > n_j$ and the channels are always relaxed before reaching the constrictions. In this case, simulations show that the variability of the times of arrest is the same as the variability introduced in the constriction size (results not shown).

This enhanced variability of the waiting time, exhibiting standard deviation up to 10 times larger than the standard deviation of the distribution of constriction sizes, is now rationalized by taking the following example. Let us consider the nth constriction in a linear channel composed of N_p constrictions and assume that this constriction is characterized by a threshold in section S_c such that $\Delta S_{c, n} = \overline{\Delta S_c}(1 + \epsilon_n)$, where $\overline{\Delta S_c}$ is the average channel deformation threshold and ϵ_n quantifies the deviation of this constriction from the average value. We consider $\epsilon_n > 0$, which holds for a constriction with a stronger blocking effect than the average, leading to stronger channel deformations ΔS_c before a jump. The new threshold can thus be expressed as

$$S_{c, n} = \bar{S}_c\left[1 - \epsilon_n\left(\frac{S_o}{\bar{S}_c} - 1\right)\right]. \tag{5.1}$$

One has to quantify its influence on the waiting time Δt. Let us suppose that the previous jump at the $(n-1)$th constriction was characterized by a threshold $\Delta S_{c, n-1} = \overline{\Delta S_c}(1 + \epsilon_{n-1})$. When $n < n_j$, the interface jumps directly from the $(n-1)$th to the nth constriction, and using the volume conservation during the jump $S_nL_n = S_{c, n-1}L_{n-1}$ leads to a cross-section of the channel equal to $S_n = S_{c, n-1}[1 + 1/(N_p - n + 1)]$.
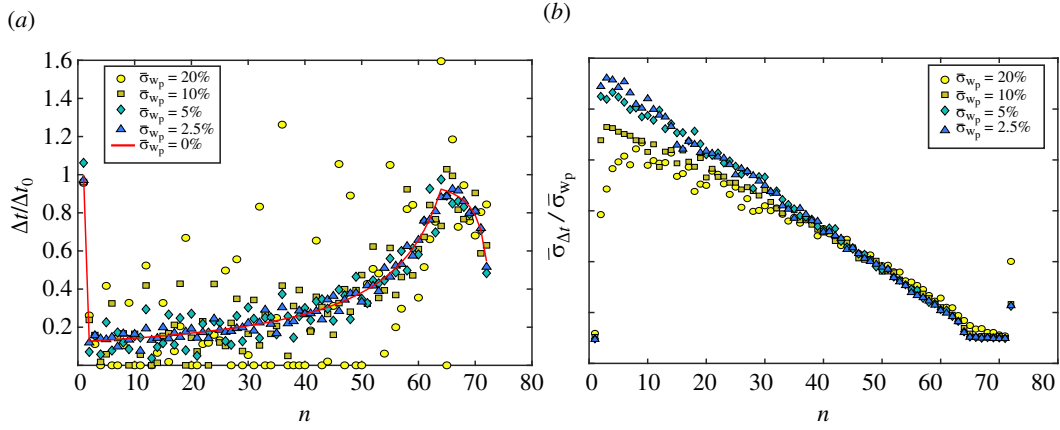
Using equation (4.2), the waiting time can therefore be expressed as

$$\Delta t = \frac{S_{c, n-1}\left(1 + \frac{1}{N_p - n + 1}\right) - S_{c, n}}{q_lL + Q_g}. \tag{5.2}$$

One can express Δt as a function of the expected waiting time $\overline{\Delta t}$ in the case without variability ($\epsilon_{n-1} = \epsilon_n = 0$), which leads to

$$\Delta t = \overline{\Delta t} - \frac{\overline{S}_c\epsilon_{n-1}\left(\frac{S_o}{\bar{S}_c} - 1\right)\left(1 + \frac{1}{N_p - n + 1}\right)}{q_lL + Q_g} + \frac{\overline{S}_c\epsilon_n\left(\frac{S_o}{\bar{S}_c} - 1\right)}{q_lL + Q_g}. \tag{5.3}$$

Finally, in the incomplete relaxation case ($1 < n < n_j$),.

figure 11. Numerical simulations. (*a*) Influence of the variability of the constriction size w_p on the waiting time Δt re-scaled by the waiting time in the absence of variability at the first constriction Δt_o, represented as a function of n for $N_p = 72$, for $\Delta S_c/S_o = 10\%$. (*b*) Dimensionless standard deviation of the waiting time $\bar{\sigma}_{\Delta t}$ divided by the dimensionless standard deviation of the constriction size σ_{w_p}, for four different sets of 1000 numerical simulations with $\overline{\sigma_{w_p}}$ varying from 20% (yellow) to 2.5% (blue).

$$\Delta t/\overline{\Delta t} = 1 - \epsilon_{n-1}\overline{\Delta S_c}/\overline{S_c}(N_p - n + 2) + \epsilon_n\overline{\Delta S_c}/\overline{S_c}(N_p - n + 1)$$

If we assume the same amplitude of variability for the section change, with a standard deviation $\sigma_{\epsilon_n} = \sigma_{\epsilon_{n-1}} = \sigma_\epsilon$, we obtain for a direct comparison with the ratio of the relative standard deviations represented in figure 11*b*

$$\frac{\Delta t/\overline{\Delta t} - 1}{\sigma_\epsilon} = \frac{\overline{\Delta S_c}}{\overline{S_c}}\left[2(N_p - n + 1) + 1\right]. \tag{5.4}$$

Physically, the amplification factor of the scattering of the waiting time compared with the scattering of the section can be understood by the fact that a slight modification of the threshold has a large effect when the pressure after the jump was very close to this threshold, see for instance the inset of figure 8*b* for large N_p. The amplification of the waiting time scattering is thus proportional to $\overline{\Delta S_c}/\overline{S_c}$, in the incomplete relaxation case. Furthermore, this amplification decays linearly with n, in agreement with the trend observed numerically. The amplification factor also increases linearly with the number of constrictions N_p, a number which can be particularly high in the leaves of some species of plants. Using equation (5.4) for the experiment with $N_p = 72$, one can estimate the variability ϵ in the blocking effect of the constrictions from the measured variability of the times of arrest Δt. Using $\Delta S_c = 0.08 S_0$ and $S_c = 0.92 S_0$, one finds $\epsilon = 12\%$, which seems reasonable regarding the apparent geometry of our 72 constrictions (figure 4*b*). Similarly, the predictions from the numerical simulations compared with the biological data from *Adiantum* (figures 2 and 10) are compatible with a standard deviation for the pit size of approximately 10% around their mean value. It could be tempting to use this as a tool to measure pit size distribution, but a larger amount of biological data are needed.

On the other hand, in cases where the pressure is completely relaxed before the interface reaches the next constriction ($n > n_j$), one has from equation (4.3): $\Delta t/\overline{\Delta t} = 1 + \epsilon$, or as a direct comparison with the ratio of the standard deviations represented in figure 11*b*

$$\frac{\Delta t/\overline{\Delta t} - 1}{\Delta S_c/\overline{\Delta S_c} - 1} = 1, \tag{5.5}$$

in agreement with the trend observed in numerical simulations: in such a case, there is no amplification of the scattering of the waiting times.

As a perspective, the leverage effect at the origin of the enhanced scattering of the characteristic time scales of embolism propagation in linear venation could lead to more complex and chaotic embolism growth in branched networks of angiosperm leaves, where the embolism can explore several competing branches and exhibit preferential paths [10,11].

5.3. Comparative analysis of biomimetic and *Adiantum* leaves

We now discuss the main differences between our biomimetic channel and *Adiantum* leaves. While some differences are acceptable as they preserve the underlying physics, others could pose limitations and motivate future improvements.

5.3.1. On the differences of pore size between the biomimetic constrictions and the pit membranes

The physical mechanisms at stake in the jerky propagation of embolism in the biomimetic leaves involve an elastocapillary coupling between the compliant structure of the PDMS channel (of Young's modulus $E \simeq 1$ MPa), and the air–water interface leading to Laplace pressure of approximately $\gamma/l_p \simeq 3$ kPa. The dimensionless elastocapillary number, defined as $E_c = E l_p/\gamma$ is

remarkably preserved across biomimetic and real leaves. Indeed, while the pores of the membrane of bordered pits are three orders of magnitude smaller than our biomimetic constrictions, the elastic modulus E of lignified tissue (whose deformation is considered as the main source of capacitance in the analogy drawn in this manuscript) is approximately three orders of magnitude larger than that of PDMS. This model of biomimetic leaves therefore preserves the potential coupling between pressure variations owing to the pits and the compliant elastic structure of the veins.

We acknowledge that in our current study, the porous structure of pit membranes, typically characterized as fibrous porous materials, was not incorporated. This simplification overlooks the complex microstructure of these membranes, which plays a crucial role in the natural process by selectively allowing water passage while blocking air, thus critically influencing embolism propagation [30,44,45]. Including such detailed structures in biomimetic models represents a significant technological challenge and an important next step for advancing our understanding. Future iterations of those biomimetic leaves could integrate these more complex features to better mimic the natural conditions and enhance the model's accuracy.

5.3.2. On the anatomical difference between the bundle of conduits in real leaves and the single veins in biomimetic leaves

The veins in real leaves consist of bundles of multiple parallel conduits. The connectivity and anatomical dimensions of these conduits have been theoretically shown to influence embolism propagation dynamics [32,46–48]. As such, in the experiments on *Adiantum*, the superposition of several parallel conduits within a single vein should theoretically yield multiple embolism events at a single network location. Figure 12*a* displays the number of registered events per pixel, illustrating that a significant portion of the leaf experiences multiple passages of embolism. Superficially, this might seem to challenge our structural model, which represents a bundle of multiple parallel conduits as a single conduit. However, if we filter the data to exclude subsequent embolisms occurring within 40 min (representing approx. one-tenth of the leaf's drying time) after the first embolism (figure 12*b*), we obtain a map more compatible with a one-dimensional front. Anatomically, this suggests that conduits surrounded by embolized veins are more likely to be rapidly embolized than others near the leading front. The front could thus be modelled as a diffuse front, with a relatively moderate spread compared with the leaf drying time scale.

5.3.3. On the poorly hygroscopic PDMS and the water transfers between the veins and the surrounding tissue

In this study, we used PDMS, a material well suited for microfabrication and capable of conveniently mimicking evapotranspiration processes owing to its pervaporation properties. However, PDMS also presents limitations owing to its inherently weakly hygroscopic nature. As a result, significant and bidirectional water transfers between the conduits and the bulk of the material—a phenomenon common in leaf tissues [41,42]—are not observed in our system. This leads us to consider the use of more hygroscopic materials in future iterations. Such materials could facilitate water exchange between the vein and the surrounding material during the cycles of pressure build-up and rapid relaxation caused by the passage of embolism through the constriction. This kind of exchange could more effectively contribute to the hydraulic capacitance required to observe the intermittent propagation patterns documented in real leaves, where our observations in biomimetic leaves have so far been based primarily on the structural deformation of the channel. While deformations of the conduit walls within the xylem are indeed present, they should not be viewed as the sole, nor probably the primary, source of hydraulic capacitance.

5.3.4. On the pressure inside the veins before embolism propagation

In our biomimetic leaves, we worked at positive pressure as the Laplace pressure jump across the curved interfaces blocked in the constriction is not strong enough to lead to negative pressures in water. This therefore prevents cavitation events and favours external air seeding scenarios where air penetrates the network from an opening (in our study, through the 'cut'). A future step forward would require the use of smaller constrictions, down to 1 µm or less, or nanoporous materials for the connection between veins, in order to achieve negative pressures, but the too soft PDMS could not sustain such a tension. Using harder materials like hydrogels could enable the creation of biomimetic leaves robust enough to sustain negative pressures without structural loss, enabling to explore the competition between cavitation and air seeding events. In addition to these improvements, using materials capable of sustaining negative pressures opens up new avenues for investigating the role of nanobubbles in the embolism-spreading phenomenon [49–51]. This exploration is particularly relevant for understanding the impact of physical chemistry, including the effects of surfactants and lipid bilayers, on the embolism dynamics within plant xylem. The inclusion of such physicochemical aspects could further refine the approach, bridging the gap between purely physical models and the more complex biological reality.

5.3.5. On the structure of the venation network and future perspectives

We focused in this study on *Adiantum* leaves, whose linear and non-reticulate venation enabled us to validate a first biomimetic chip as a promising physics-based tool. Future studies could explore dynamics in more complex reticulate networks where embolism could follow various paths and invade veins of different sizes (and various network 'orders', as mentioned by Brodribb *et al.* [10]). In particular, connections between veins across the network could be tested and confronted to dynamical and anatomical observations in real leaves. The development and refinement of this biomimetic reticulate network will provide an ideal experimental platform to test, confront and refine theoretical models that predict embolism spreading, offering a valuable bridge between empirical observations and simulation-based forecasts [32,46–48].

(a)

(b)
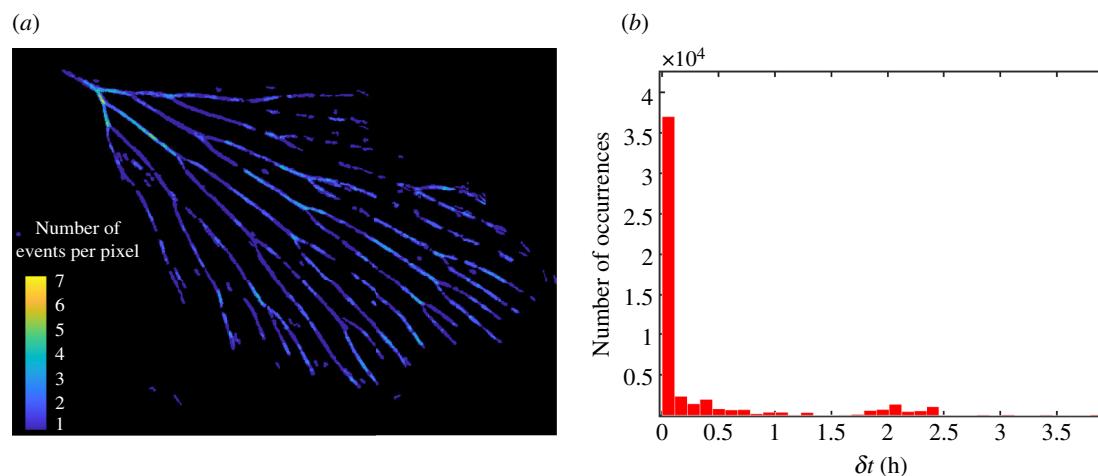
figure 12. Analysis carried out from the data shared by the authors of reference [10], courtesy of Timothy Brodribb *et al.* (*a*) Multiple embolism events can be detected, ranging from 1 to 7 per pixel. (*b*) Histogram of the time differences $\delta t = t - t_0$ between the time of each embolism detection t and the first detection t_0, for a given pixel on the image. It is important to note that most of those multiple embolisms events occurs less than ten minutes after the first embolism.

6. Conclusion and perspectives

In this study, we expanded upon our recent observations of jerky embolism propagation induced by a single biomimetic constriction [29], developing a model with linear biomimetic vessels composed of regularly spaced constrictions. We identified two distinct dynamics based on the pressure state at the moment an embolism encounters a constriction. If the pressure is fully relaxed, characteristic of small channel deformations or short conduit lengths, the waiting time aligns with predictions for a single constriction [29]. Conversely, if the pressure is only partially relaxed, the resulting waiting times are more complex and vary with the size and order of the constrictions. In this case, an increased variability originating from a leverage effect, owing to the incomplete elastic relaxation within the compliant hydraulic network of the channels, was evidenced.

The biomimetic model we developed, despite its simplicity, effectively captures the fundamental intermittent dynamics of embolism propagation observed in *Adiantum* leaves. By strategically simplifying complex biological aspects—such as hydraulic capacitance, the structure of bordered pit membranes, pressure conditions and the anatomical features of the xylem—our model maintains tractability for systematic parametric studies. This approach not only facilitates a deeper understanding of plant hydraulics but also sets the stage for future studies that aim to refine theoretical models through empirical validation. In addition, this biomimetic tool is transparent, reusable, easy to fabricate and yields robust results. Its versatility and simplicity make it ideal for parametric studies, and it is designed to accommodate incremental modifications to gradually include more complex factors such as varied pressure conditions, xylem anatomy and constriction structures, thus enhancing its applicative scope in plant hydraulic studies.

Looking forward, the biomimetic samples presented in this study could be adapted to explore two-dimensional reticulate networks, potentially unravelling new physical and biological insights. One open question is whether the trajectory of embolism growth is stochastic or deterministic, which influences the observed patterns of embolism propagation and hierarchical dynamics in drying leaves [10,11]. Addressing these questions will clarify the underlying mechanisms that dictate embolism pathways and their impacts on plant health and survival.

References

1. Tyree MT, Zimmermann MH. 2013 *Xylem structure and the ascent of sap*. Heidelberg, Germany: Springer Science & Business Media.

2. Venturas MD, Sperry JS, Hacke UG. 2017 Plant xylem hydraulics: what we understand, current research, and future challenges. *J. Integr. Plant Biol.* **59**, 356–389. (doi:10.1111/jipb.12534)

3. Brodribb T, Brodersen CR, Carriqui M, Tonet V, Rodriguez Dominguez C, McAdam S. 2021 Linking xylem network failure with leaf tissue death. *New Phytol.* **232**, 68–79. (doi:10.1111/nph.17577)

4. Choat B *et al*. 2012 Global convergence in the vulnerability of forests to drought. *Nature* **491**, 752–755. (doi:10.1038/nature11688)

5. Choat B, Brodribb TJ, Brodersen CR, Duursma RA, López R, Medlyn BE. 2018 Triggers of tree mortality under drought. *Nature* **558**, 531–539. (doi:10.1038/s41586-018-0240-x)

6. Brodribb TJ, Powers J, Cochard H, Choat B. 2020 Hanging by a thread? Forests and drought. *Science* **368**, 261–266. (doi:10.1126/science.aat7631)

7. Choat B, Drayton WM, Brodersen C, Matthews MA, Shackel KA, Wada H, McElrone AJ. 2010 Measurement of vulnerability to water stress-induced cavitation in grapevine: a comparison of four techniques applied to a long-vesseled species. *Plant Cell Environ.* **33**, 1502–1512. (doi:10.1111/j.1365-3040.2010.02160.x)

8. Cochard H, Delzon S, Badel E. 2015 X-ray microtomography (micro-CT): a reference technology for high-resolution quantification of xylem embolism in trees. *Plant Cell Environ.* **38**, 201–206. (doi:10.1111/pce.12391)

9. Fukuda K, Kawaguchi D, Aihara T, Ogasa MY, Miki NH, Haishi T, Umebayashi T. 2015 Vulnerability to cavitation differs between current-year and older xylem: non-destructive observation with a compact magnetic resonance imaging system of two deciduous diffuse-porous species. *Plant Cell Environ.* **38**, 2508–2518. (doi:10.1111/pce.12510)

10. Brodribb TJ, Bienaimé D, Marmottant P. 2016 Revealing catastrophic failure of leaf networks under stress. *Proc. Natl Acad. Sci. USA* **113**, 4865–4869. (doi:10.1073/pnas.1522569113)

11. Brodribb TJ, Skelton RP, McAdam SAM, Bienaimé D, Lucani CJ, Marmottant P. 2016 Visual quantification of embolism reveals leaf vulnerability to hydraulic failure. *New Phytol.* **209**, 1403–1409. (doi:10.1111/nph.13846)

12. Rodriguez-Dominguez CM, Carins Murphy MR, Lucani C, Brodribb TJ. 2018 Mapping xylem failure in disparate organs of whole plants reveals extreme resistance in olive roots. *New Phytol.* **218**, 1025–1035. (doi:10.1111/nph.15079)

13. Brodribb TJ, Carriqui M, Delzon S, Lucani C. 2017 Optical measurement of stem xylem vulnerability. *Plant Physiol.* **174**, 2054–2061. (doi:10.1104/pp.17.00552)

14. Harrison Day BL, Carins-Murphy MR, Brodribb TJ. 2022 Reproductive water supply is prioritized during drought in tomato. *Plant Cell Environ.* **45**, 69–79. (doi:10.1111/pce.14206)

15. Penvern H *et al*. 2020 How bound water regulates wood drying. *Phys. Rev. Appl.* **14**, 054051. (doi:10.1103/PhysRevApplied.14.054051)

16. Cocusse M, Rosales M, Maillet B, Sidi-Boulenouar R, Julien E, Caré S, Coussot P. 2022 Two-step diffusion in cellular hygroscopic (vascular plant-like) materials. *Sci. Adv.* **8**, eabm7830. (doi:10.1126/sciadv.abm7830)

17. Jensen K, Forterre Y. 2022 *Soft matter in plants: from biophysics to biomimetics*. vol. **15**. Cambridge, UK: Royal Society of Chemistry.

18. Noblin X, Mahadevan L, Coomaraswamy IA, Weitz DA, Holbrook NM, Zwieniecki MA. 2008 Optimal vein density in artificial and real leaves. *Proc. Natl Acad. Sci. USA* **105**, 9140–9144. (doi:10.1073/pnas.0709194105)

19. Jensen KH, Rio E, Hansen R, Clanet C, Bohr T. 2009 Osmotically driven pipe flows and their relation to sugar transport in plants. *J. Fluid Mech.* **636**, 371–396. (doi:10.1017/S002211200900799X)

20. Comtet J, Jensen KH, Turgeon R, Stroock AD, Hosoi AE. 2017 Passive phloem loading and long-distance transport in a synthetic tree-on-a-chip. *Nat. Plants* **3**, 1–8. (doi:10.1038/nplants.2017.32)

21. Wheeler TD, Stroock AD. 2008 The transpiration of water at negative pressures in a synthetic tree. *Nature* **455**, 208–212. (doi:10.1038/nature07226)

22. Vincent O, Marmottant P, Quinto-Su PA, Ohl CD. 2012 Birth and growth of cavitation bubbles within water under tension confined in a simple synthetic tree. *Phys. Rev. Lett.* **108**, 184502. (doi:10.1103/PhysRevLett.108.184502)

23. Duan C, Karnik R, Lu MC, Majumdar A. 2012 Evaporation-induced cavitation in nanofluidic channels. *Proc. Natl Acad. Sci. USA* **109**, 3688–3693. (doi:10.1073/pnas.1014075109)

24. Vincent O, Marmottant P. 2017 On the statics and dynamics of fully confined bubbles. *J. Fluid Mech.* **827**, 194–224. (doi:10.1017/jfm.2017.487)

25. Bruning MA, Costalonga M, Snoeijer JH, Marin A. 2019 Turning drops into bubbles: cavitation by vapor diffusion through elastic networks. *Phys. Rev. Lett.* **123**, 214501. (doi:10.1103/PhysRevLett.123.214501)

26. Dollet B, Louf JF, Alonzo M, Jensen KH, Marmottant P. 2019 Drying of channels by evaporation through a permeable medium. *J. R. Soc. Interface* **16**, 20180690. (doi:10.1098/rsif.2018.0690)

27. Chagua Encarnación KN, Marmottant P, Dollet B. 2021 Pervaporation-induced drying in networks of channels of variable width. *Microfluid. Nanofluid.* **25**, 71. (doi:10.1007/s10404-021-02467-2)

28. Dollet B, Chagua Encarnación KN, Gautier R, Marmottant P. 2021 Drying by pervaporation in elementary channel networks. *J. Fluid Mech.* **906**, A6. (doi:10.1017/jfm.2020.794)

29. Keiser L, Marmottant P, Dollet B. 2022 Intermittent air invasion in pervaporating compliant microchannels. *J. Fluid Mech.* **948**, A52. (doi:10.1017/jfm.2022.733)

30. Zhang Y, Pereira L, Kaack L, Liu J, Jansen S. 2024 Gold perfusion experiments support the multi-layered, mesoporous nature of intervessel pit membranes in angiosperm xylem. *New Phytol.* **242**, 493–506. (doi:10.1111/nph.19608)

31. McCulloh KA, Sperry JS, Adler FR. 2003 Water transport in plants obeys Murray's law. *Nature* **421**, 939–942. (doi:10.1038/nature01444)

32. Loepfe L, Martinez-Vilalta J, Piñol J, Mencuccini M. 2007 The relevance of xylem network structure for plant hydraulic efficiency and safety. *J. Theor. Biol.* **247**, 788–803. (doi:10.1016/j.jtbi.2007.03.036)

33. Wason J, Bouda M, Lee EF, McElrone AJ, Phillips RJ, Shackel KA, Matthews MA, Brodersen C. 2021 Xylem network connectivity and embolism spread in grapevine (*Vitis vinifera* L.). *Plant Physiol.* **186**, 373–387. (doi:10.1093/plphys/kiab045)

34. Bacchin P, Leng J, Salmon JB. 2022 Microfluidic evaporation, pervaporation, and osmosis: from passive pumping to solute concentration. *Chem. Rev.* **122**, 6938–6985. (doi:10.1021/acs.chemrev.1c00459)

35. Cochard H, Froux F, Mayr S, Coutand C. 2004 Xylem wall collapse in water-stressed pine needles. *Plant Physiol.* **134**, 401–408. (doi:10.1104/pp.103.028357)

36. Brodribb TJ, Holbrook NM. 2005 Water stress deforms tracheids peripheral to the leaf vein of a tropical conifer. *Plant Physiol.* **137**, 1139–1146. (doi:10.1104/pp.104.058156)

37. Blackman CJ, Brodribb TJ, Jordan GJ. 2010 Leaf hydraulic vulnerability is related to conduit dimensions and drought resistance across a diverse range of woody angiosperms. *New Phytol.* **188**, 1113–1123. (doi:10.1111/j.1469-8137.2010.03439.x)

38. Zhang YJ, Rockwell FE, Graham AC, Alexander T, Holbrook NM. 2016 Reversible leaf xylem collapse: a potential 'circuit breaker' against cavitation. *Plant Physiol.* **172**, 2261–2274. (doi:10.1104/pp.16.01191)

39. Corso D, Delzon S, Lamarque LJ, Cochard H, Torres-Ruiz JM, King A, Brodribb TJ. 2020 Neither xylem collapse, cavitation, or changing leaf conductance drive stomatal closure in wheat. *Plant Cell Environ.* **43**, 854–865. (doi:10.1111/pce.13722)

40. Chin ARO, Guzmán-Delgado P, Sillett SC, Kerhoulas LP, Ambrose AR, McElrone AR, Zwieniecki MA. 2022 Tracheid buckling buys time, foliar water uptake pays it back: coordination of leaf structure and function in tall redwood trees. *Plant Cell Environ.* **45**, 2607–2616. (doi:10.1111/pce.14381)

41. Sack L, Holbrook NM. 2006 Leaf hydraulics. *Annu. Rev. Plant Biol.* **57**, 361–381. (doi:10.1146/annurev.arplant.56.032604.144141)

42. Blackman CJ, Brodribb TJ. 2011 Two measures of leaf capacitance: insights into the water transport pathway and hydraulic conductance in leaves. *Funct. Plant Biol.* **38**, 118–126. (doi:10.1071/FP10183)

43. Ma X, Maillet B, Brochard L, Pitois O, Sidi-Boulenouar R, Coussot P. 2022 Vapor-sorption coupled diffusion in cellulose fiber pile revealed by magnetic resonance imaging. *Phys. Rev. Appl.* **17**, 024048. (doi:10.1103/PhysRevApplied.17.024048)

44. Kaack L *et al*. 2021 Pore constrictions in intervessel pit membranes provide a mechanistic explanation for xylem embolism resistance in angiosperms. *New Phytol.* **230**, 1829–1843. (doi:10.1111/nph.17282)

45. Zhang Y *et al*. 2020 High porosity with tiny pore constrictions and unbending pathways characterize the 3D structure of intervessel pit membranes in angiosperm xylem. *Plant Cell Environ.* **43**, 116–130. (doi:10.1111/pce.13654)

46. Roth-Nebelsick A. 2019 It's contagious: calculation and analysis of xylem vulnerability to embolism by a mechanistic approach based on epidemic modeling. *Trees* **33**, 1519–1533. (doi:10.1007/s00468-019-01891-w)

47. Mrad A, Johnson DM, Love DM, Domec JC. 2021 The roles of conduit redundancy and connectivity in xylem hydraulic functions. *New Phytol.* **231**, 996–1007. (doi:10.1111/nph.17429)

48. Roth-Nebelsick A, Konrad W. 2023 Modeling and analyzing xylem vulnerability to embolism as an epidemic process. In *Xylem: methods and protocols* (ed. J Agusti), pp. 17–34. New York, NY: Springer. (doi:10.1007/978-1-0716-3477-6)

49. Schenk HJ, Steppe K, Jansen S. 2015 Nanobubbles: a new paradigm for air-seeding in xylem. *Trends Plant Sci.* **20**, 199–205. (doi:10.1016/j.tplants.2015.01.008)

50. Kanduč M, Schneck E, Loche P, Jansen S, Schenk HJ, Netz RR. 2020 Cavitation in lipid bilayers poses strict negative pressure stability limit in biological liquids. *Proc. Natl Acad. Sci. USA* **117**, 10 733–10 739. (doi:10.1073/pnas.1917195117)

51. Ingram S, Jansen S, Schenk HJ. 2023 Lipid-coated nanobubbles in plants. *Nanomaterials* **13**, 1776. (doi:10.3390/nano13111776)

52. Keiser L, Dollet B, Marmottant P. 2024 Data from: Embolism propagation in adiantum leaves and in a biomimetic system with constrictions. Zenodo. (doi:10.5281/zenodo.11206159)